



# Mace-like carbon fibers@Fe<sub>3</sub>O<sub>4</sub>@carbon composites as anode materials for lithium-ion batteries

Shaowei Yao<sup>1,2</sup> · Guifang Zhang<sup>1</sup> · Xingxiang Zhang<sup>1</sup> · Zhiqiang Shi<sup>1</sup>

Received: 30 May 2020 / Revised: 9 August 2020 / Accepted: 20 August 2020 / Published online: 30 August 2020  
© Springer-Verlag GmbH Germany, part of Springer Nature 2020

## Abstract

Mace-like carbon fibers@Fe<sub>3</sub>O<sub>4</sub>@carbon (CF@Fe<sub>3</sub>O<sub>4</sub>@C) composites were designed and synthesized via an in situ growth and carbon coating approach with heat treatment. In comparison with CF, Fe<sub>2</sub>O<sub>3</sub>, and CF@Fe<sub>2</sub>O<sub>3</sub>, CF@Fe<sub>3</sub>O<sub>4</sub>@C composites exhibit higher electrochemical performance as anode materials for lithium-ion batteries (LIBs), owing to the unique mace-like ordered structure. Mace-like CF@Fe<sub>3</sub>O<sub>4</sub>@C composites deliver a high discharge/charge specific capacities of 1368/940 mAh g<sup>-1</sup> at the first cycle and 741/740 mAh g<sup>-1</sup> at the 100th cycles at 100 mA g<sup>-1</sup> in the range of 0.01–2.5 V. The specific discharge capacity can still retain 503 mAh g<sup>-1</sup> after 500 cycles at 500 mA g<sup>-1</sup>. The outstanding electrochemical performance can be attributed to that carbon fibers and carbon coating improve the electrical conductivity of iron oxides and the carbon-coated layer avoids the specific capacity fading caused by volume expansion of iron oxides during charging/discharging. It provides a novel structural design strategy and an effective synthesis method of anode material for high-energy lithium-ion battery.

**Keywords** Iron oxide · Carbon fibers · Carbon coating · Lithium-ion batteries

## Introduction

Lithium-ion batteries have the characteristics of high specific energy, high specific power, high open-circuit voltage, stable discharge, large working range, and long service life [1]. As LIBs are being more and more widely used, it becomes inseparable from our life [2, 3]. Scientists hope to develop LIBs with higher capacity, longer cycle stability, lower cost, and greater safety. Therefore, it is important to develop electrode materials with better performance.

At the beginning of the twenty-first century, Tarascon's [4] group first discovered the potential of transition metal oxides (TMOs) as anode materials for LIBs. Iron oxides have been

widely studied as anode materials, because of rich resources, no pollution to the environment, and especially relatively high specific capacity ( $\alpha$ -Fe<sub>2</sub>O<sub>3</sub> is 1007 mAh g<sup>-1</sup>, Fe<sub>3</sub>O<sub>4</sub> is 926 mAh g<sup>-1</sup>). But there are two shortcomings: one is poor conductivity and the other one is large volume changes during charge/discharge cycles leading to fast capacity fading. The  $\alpha$ -Fe<sub>2</sub>O<sub>3</sub>-CNTs architectures synthesized by the hydrothermal method as anode materials can ensure the fast electronic transmission paths and improve electronic conductivity and the rate performance of electrode materials [5]. Ni(OH)<sub>2</sub>-Fe<sub>2</sub>O<sub>3</sub>/onion-like nano-carbon composites were prepared by Dwivedi's [6] group through a liquid-phase precipitation method and hydrothermal synthesis.

The design idea of experiment mainly comes from the following three parts. First, in order to improve the shortcomings of poor conductivity of electrode materials, a large specific capacity iron oxide (Fe<sub>2</sub>O<sub>3</sub>) in situ grows on the carbon fiber (CF) surface to form an iron oxide carbon fiber composite material (CF@Fe<sub>2</sub>O<sub>3</sub>). Second, CF@Fe<sub>2</sub>O<sub>3</sub> is treated by carbon coating to obtain CF@Fe<sub>3</sub>O<sub>4</sub>@C, expecting that the surface carbon layer will increase its conductivity and buffer large volume changes during Li<sup>+</sup> insertion/extraction. Third, the pore structure of electrode materials can be improved to shorten the diffusion distance of lithium ions, alleviate the volume change, and maintain the structural stability. In short,

✉ Guifang Zhang  
zhangguifang@tjpu.edu.cn

✉ Zhiqiang Shi  
shizhiqiang@tiangong.edu.cn

<sup>1</sup> Tianjin Municipal Key Laboratory of Advanced Fiber and Energy Storage Technology, School of Material Science and Engineering, Tiangong University, Tianjin 300387, People's Republic of China

<sup>2</sup> Key Laboratory of Inorganic Material of Hebei Province, College of Material Science and Engineering, North China University of Science and Technology, Tangshan 063210, Hebei, People's Republic of China

it not only retains the advantages of high specific capacity of iron oxide but also makes up for its disadvantages of poor conductivity and severe capacity degradation, exploring its potential as an anode electrode material for LIBs.

## Experimental section

### Synthesis of CF

Polyacrylonitrile (PAN, 3 g) was dissolved in 28 mL of *N,N*-dimethylformamide (DMF) to obtain electrospinning solution, and then the solution was filled into a syringe. The needle was about 15 cm from the collector; the voltage was 20 kV. Electrospun fibers were collected, dried, and placed in an electric furnace at 250 °C for 4 h. Then, the fibers were transferred into a tube furnace and heated to 700 °C at heating rate of 2 °C min<sup>-1</sup> under N<sub>2</sub> atmosphere; the temperature of 700 °C was maintained for 2 h. After cooling, black carbon fibers (CF) were obtained.

### Synthesis of Fe<sub>2</sub>O<sub>3</sub>

In total, 2.7 g of FeCl<sub>3</sub>·6H<sub>2</sub>O was dissolved in 100 mL of deionized water which was magnetically stirred for 2 h in an oil bath at 80 °C. Samples were collected after static settlement 12 h, washed by distilled water three times, and dried for 12 h at 60 °C in an electronic oven. Then, samples were heat-treated at 400 °C for 4 h in an electric furnace with heating rate of 2 °C min<sup>-1</sup>, and red-brown samples were obtained after cooling down with the furnace.

### Synthesis of CF@Fe<sub>2</sub>O<sub>3</sub> and CF@Fe<sub>3</sub>O<sub>4</sub>@C

Two grams of CF was added into 60 mL of concentrated nitric acid, magnetically stirred at 65 °C for 2 h, separated by centrifugation, washed with deionized water to pH = 7, and dried for 12 h at 80 °C. FeCl<sub>3</sub>·6H<sub>2</sub>O (2.16 g) and the above CF (0.1 g) were dissolved with 60 mL of deionized water with magnetic stirring for 5 h under 75 °C in water bath. Then, the samples were separated by centrifugation, washed with deionized water three times, dried at 80 °C for 12 h, and heated to 400 °C for 4 h at heating rate of 2 °C min<sup>-1</sup> to obtain CF@Fe<sub>2</sub>O<sub>3</sub>. Fifty milligrams of dopamine hydrochloride and 100 mg CF@Fe<sub>2</sub>O<sub>3</sub> were put in 42.5 mL of Tris buffer solution (pH = 8.5), and the solution was continuously stirred for 18 h at room temperature. The obtained CF@Fe<sub>2</sub>O<sub>3</sub>@dopamine samples were collected by centrifugation, washed three times with water, and dried at 80 °C for 12 h. Finally, the CF@Fe<sub>2</sub>O<sub>3</sub>@dopamine samples were put into the tube furnace under N<sub>2</sub> atmosphere, then heated to 580 °C at a rate of 2 °C min<sup>-1</sup> and maintained for 2 h to obtain CF@Fe<sub>3</sub>O<sub>4</sub>@C.

The synthetic procedure for mace-like CF@Fe<sub>3</sub>O<sub>4</sub>@C composites is shown in Fig. 1. Iron oxide electrode materials have poor conductivity, while CF have good conductivity [7, 8]. To improve the electrical conductivity, CF would be compounded with iron oxides. First, the heat-treated CF were processed with nitric acid solution to add functional groups such as –OH and –COOH. Furthermore, FeOOH in situ grew on the surface of the carbon fibers in water bath, and then CF@Fe<sub>2</sub>O<sub>3</sub> was obtained by heat treatment. Finally, CF@Fe<sub>2</sub>O<sub>3</sub> coated with dopamine hydrochloride was heat-treated to obtain CF@Fe<sub>3</sub>O<sub>4</sub>@C.

### Material characterization

TGA (STA449F5, NETZSCH) of sample was tested with a heating rate of 5 °C min<sup>-1</sup> in the range of 40–800 °C under air condition. The crystal structures were investigated by X-ray diffraction (XRD, D/MAX2500PC, RIGAKU, with Cu-K $\alpha$  radiation,  $\lambda = 1.54178 \text{ \AA}$ ) in 10 to 80°. The surface chemical properties of CF@Fe<sub>3</sub>O<sub>4</sub>@C were evaluated by X-ray photoelectron spectra (XPS, Thermo ESCALAB 250XI). Raman spectra and Fourier transform infrared (FT-IR) analysis of samples were carried out using Raman spectroscopy (DXR, Thermo Fisher Scientific, with a 632.8-nm laser) and FT-IR spectroscopy (VERTEX70, Bruker, with a resolution of 2 cm<sup>-1</sup>), respectively. N<sub>2</sub> adsorption/desorption measurements were performed by a Quantachrome instrument (QUADRASORB, SI-MP) at 77 K. The morphological characteristics of the samples were observed by scanning electron microscopy (SEM, Scios, FEI) and transmission electron microscopy (TEM, JEM-2800, JEOL) with an accelerating voltage of 200 kV.

### Electrochemical measurement

In order to investigate the electrochemical performance of CF@Fe<sub>3</sub>O<sub>4</sub>@C composite, the active material, acetylene black, and PVDF were mixed according to a mass ratio of 7:1.5:1.5 with NMP. Then, the mixture was coated on a copper foil collector. After drying, it was made into a circular piece with the active material loading about 1–2 mg cm<sup>-2</sup>. The button-type CR2032 half-cell was assembled in an argon glove box with metal lithium foil as the counter electrode, Celgard 2400 as the separator, and water and oxygen content below 0.1 ppm respectively. The electrolyte was 1.0 M LiPF<sub>6</sub> in EC/DMC/DEC (1:1:1 in volume). At room temperature, discharge and charge performances of cells were tested on Land CT2001A in the cut-off voltage 0.01–2.5 V (vs. Li<sup>+</sup>/Li). Cyclic voltammetry (CV) was performed at the scan rate of 0.1 mV s<sup>-1</sup> in 0–3 V (vs. Li<sup>+</sup>/Li) on the PGSTAT204 electrochemical workstation. Electrochemical impedance spectroscopy (EIS) was conducted in the frequency range of 0.1–10<sup>6</sup> Hz. To have a better comparison, CF, Fe<sub>2</sub>O<sub>3</sub>, and

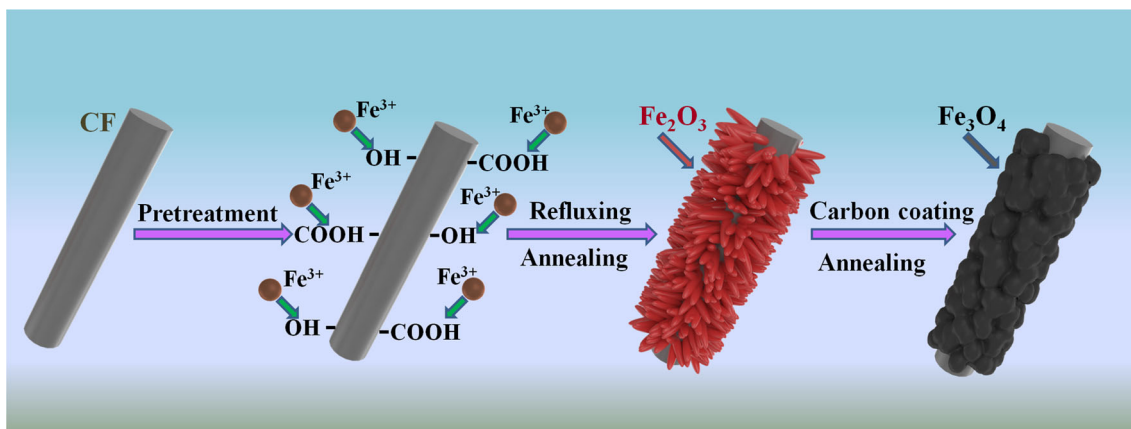


Fig. 1 Schematic illustration of synthetic CF@Fe<sub>3</sub>O<sub>4</sub>@C

CF@Fe<sub>2</sub>O<sub>3</sub> were also experimented for the electrochemical performances.

### Results and discussion

The TG curves of CF, Fe<sub>2</sub>O<sub>3</sub>, CF@Fe<sub>2</sub>O<sub>3</sub>, and CF@Fe<sub>3</sub>O<sub>4</sub>@C precursors are shown in Fig. 2a. The total mass loss values of CF, Fe<sub>2</sub>O<sub>3</sub>, CF@Fe<sub>2</sub>O<sub>3</sub>, and CF@Fe<sub>3</sub>O<sub>4</sub>@C are 99.5%, 21.8%, 85.2%, and 67.4%, respectively. Taking CF@Fe<sub>3</sub>O<sub>4</sub>@C as an example, the mass loss from 40 to 220 °C (about 4.9%) is mainly due to the removal of adsorbed water and crystal water. With temperature increasing, the subsequent mass loss (62.5%) from 220 to 580 °C can be attributed to the decomposition of dopamine hydrochloride [9, 10]. It can be considered that the stable CF@Fe<sub>3</sub>O<sub>4</sub>@C composite has formed because of the mass loss no longer changing after exceeding 580 °C. The carbon contents of CF@Fe<sub>2</sub>O<sub>3</sub> and CF@Fe<sub>3</sub>O<sub>4</sub>@C are 85.2% and 67.4% according to the results by TG measurement.

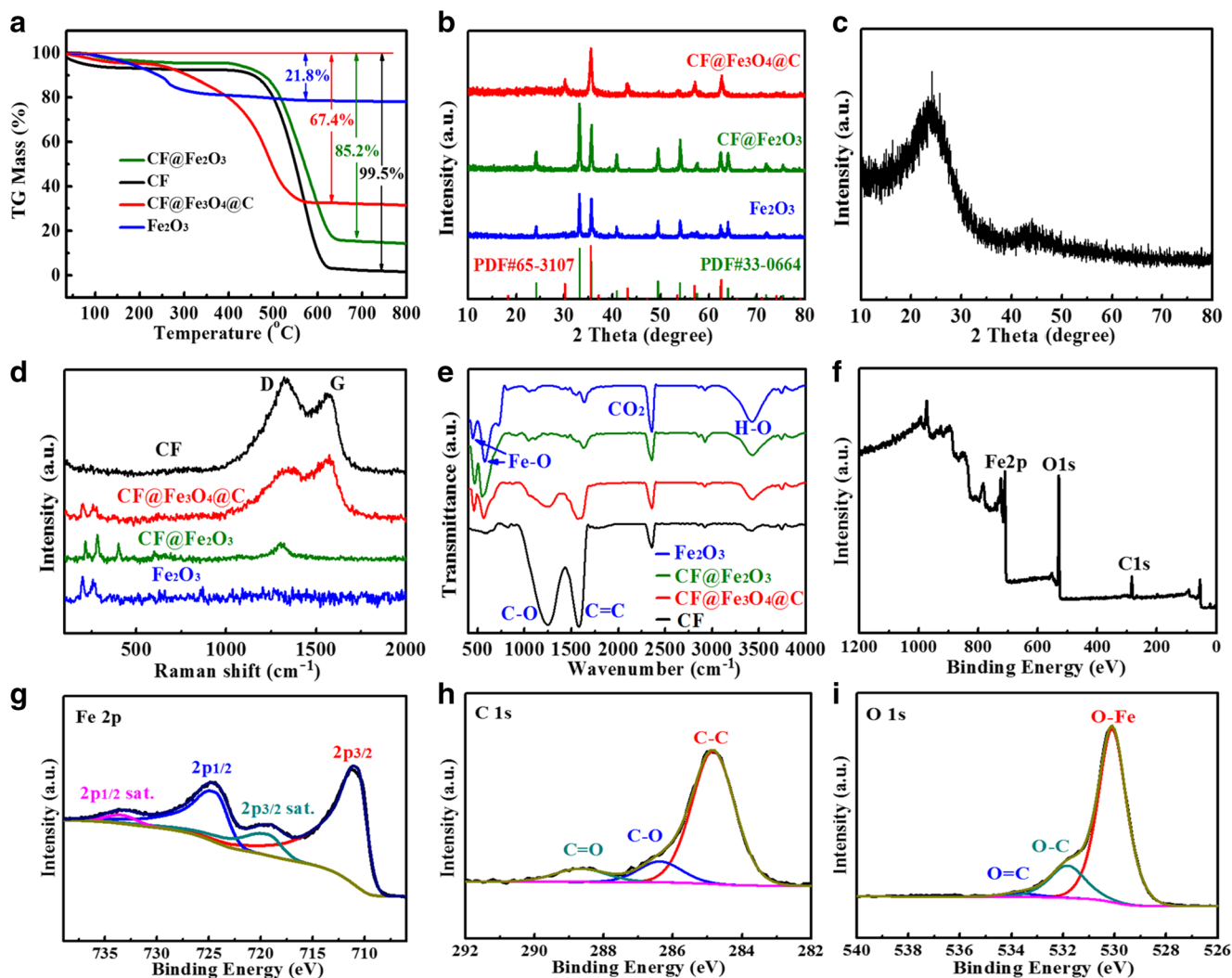
Figure 2b shows the XRD patterns of Fe<sub>2</sub>O<sub>3</sub>, CF@Fe<sub>2</sub>O<sub>3</sub>, and CF@Fe<sub>3</sub>O<sub>4</sub>@C. It can be seen that the main diffraction peaks of spindle-shaped Fe<sub>2</sub>O<sub>3</sub> and CF@Fe<sub>2</sub>O<sub>3</sub> are consistent with α-Fe<sub>2</sub>O<sub>3</sub> standard card (PDF#33-0664), such as the diffraction peaks at 24.1°, 33.2°, 35.6°, 49.5°, 54.1°, 62.4°, and 64.0°, corresponding to (012), (104), (110), (024), (116), (214), and (300) of α-Fe<sub>2</sub>O<sub>3</sub>, respectively. The crystal plane is a hexagonal crystal structure, and its space group is R-3C (167) (*a* = *b* = 5.0356 Å, *c* = 13.7489 Å) [11, 12]. The main diffraction peaks of CF@Fe<sub>3</sub>O<sub>4</sub>@C are consistent with the Fe<sub>3</sub>O<sub>4</sub> standard card (PDF#65-3107), such as the diffraction peaks at 30.1°, 35.5°, 43.1°, 53.5°, 57.0°, 62.6°, and 74.0° that correspond to (220), (311), (400), (422), (511), (440), and (533) of Fe<sub>3</sub>O<sub>4</sub>, respectively. The crystal plane is a cubic crystal structure and the space group is Fd-3m (227) (*a* = *b* = *c* = 8.3905 Å) [13, 14], indicating that the phase of Fe<sub>3</sub>O<sub>4</sub> is obtained from CF@Fe<sub>2</sub>O<sub>3</sub> coated with dopamine hydrochloride after heat treatment. The XRD results of CF are shown in

Fig. 2c. Obvious peaks at 26° and 44° are the characteristic peaks of amorphous carbon, indicating that polyacrylonitrile has transformed into CF after heat treatment.

The Raman spectra of CF, Fe<sub>2</sub>O<sub>3</sub>, CF@Fe<sub>2</sub>O<sub>3</sub>, and CF@Fe<sub>3</sub>O<sub>4</sub>@C are given in Fig. 2d. For the spectra of Fe<sub>2</sub>O<sub>3</sub>, CF@Fe<sub>2</sub>O<sub>3</sub>, and CF@Fe<sub>3</sub>O<sub>4</sub>@C, there are some obvious peaks between 200 and 800 cm<sup>-1</sup>, such as the peaks at 220, 286, 402, 490, and 602 cm<sup>-1</sup>, which should be attributed to the characteristic scattering peaks of Fe<sub>2</sub>O<sub>3</sub> and Fe<sub>3</sub>O<sub>4</sub> [15–18]. Meanwhile, the spectrum of CF only shows two strong peaks near 1350 and 1560 cm<sup>-1</sup>, which are attributed to the D and G peaks of graphitized carbon. In addition, the sample CF@Fe<sub>2</sub>O<sub>3</sub> appears a strong peak at 1350 cm<sup>-1</sup>, which should be a characteristic peak of carbon fiber. While CF@Fe<sub>3</sub>O<sub>4</sub>@C demonstrates two peaks at 1350 and 1560 cm<sup>-1</sup>, which should be attributed to the D and G peaks of the carbon fiber and the coated carbon layer, representing the presence of carbon with a disordered graphite composite structure [19, 20].

The functional groups of CF, Fe<sub>2</sub>O<sub>3</sub>, CF@Fe<sub>2</sub>O<sub>3</sub>, and CF@Fe<sub>3</sub>O<sub>4</sub>@C were clarified by Fourier transform infrared transmittance spectra, as seen in Fig. 2e. For the spectra, strong peaks at 3416, 2357, 1630, 1541, 1026, 575, and 446 cm<sup>-1</sup> are obvious. The peak at 3416 cm<sup>-1</sup> is a stretching vibration peak of –OH, which is the absorption peak of absorbed water [21, 22], and the peak at 2357 cm<sup>-1</sup> is the absorption peak of CO<sub>2</sub> in the air. The peak at 1630 cm<sup>-1</sup> may be the hydroxyl bending vibration peak of water, and the bands at 1541 cm<sup>-1</sup> and 1026 cm<sup>-1</sup> are attributed to the C=C and C–O stretching, respectively. For the curves of Fe<sub>2</sub>O<sub>3</sub>, CF@Fe<sub>2</sub>O<sub>3</sub>, and CF@Fe<sub>3</sub>O<sub>4</sub>@C, the peaks at 574 cm<sup>-1</sup> and 449 cm<sup>-1</sup>, 549 cm<sup>-1</sup> and 468 cm<sup>-1</sup>, and 563 cm<sup>-1</sup> and 462 cm<sup>-1</sup> belong to the absorption of Fe–O [22, 23]. This indicates the existence of iron oxides and also accords with the results of XRD and Raman.

To further determine the surface electron valence and chemical composition of CF@Fe<sub>3</sub>O<sub>4</sub>@C, X-ray photoelectron spectroscopy (XPS) was performed. The survey spectrum



**Fig. 2** a TG curves of CF, Fe<sub>2</sub>O<sub>3</sub>, CF@Fe<sub>2</sub>O<sub>3</sub>, and CF@Fe<sub>3</sub>O<sub>4</sub>@C; XRD patterns of (b) Fe<sub>2</sub>O<sub>3</sub>, CF@Fe<sub>2</sub>O<sub>3</sub>, and CF@Fe<sub>3</sub>O<sub>4</sub>@C; and (c) CF; (d) Raman spectra and (e) FT-IR spectra of CF, Fe<sub>2</sub>O<sub>3</sub>,

CF@Fe<sub>2</sub>O<sub>3</sub>, and CF@Fe<sub>3</sub>O<sub>4</sub>@C; XPS of CF@Fe<sub>3</sub>O<sub>4</sub>@C: (f) survey spectrum and high-resolution spectra of (g) Fe 2p, (h) C 1s, and (i) O 1s

and the high-resolution spectra of Fe 2p, C 1s, and O 1s are shown in Fig. 2f–i. It can be seen that characteristic peaks of the elements Fe, C, and O are exhibited in the ranges of 705–740, 282–292, and 256–240 eV, respectively. The results of XPS are consistent with those of XRD, Raman, and FT-IR. For Fig. 2g, the existence of iron ion in C@Fe<sub>3</sub>O<sub>4</sub>@C can be determined by the characteristic peaks of Fe2p<sub>3/2</sub> and Fe2p<sub>1/2</sub> at 711.1 and 725.0 eV, respectively. At the same time, the satellite peaks at 720.1 and 733.7 eV correspond to Fe2p<sub>3/2</sub> Sat. and Fe2p<sub>1/2</sub> Sat., respectively, also proving the existence of iron ion. The spectrum of C 1s is shown in Fig. 2h; the peaks at 284.8, 286.4, and 288.7 eV correspond to graphite C–C, C–O, and C=O, respectively. As can be seen from Fig. 2i about the O 1s spectrum, the peak at 530.1 eV corresponds to O–Fe, further confirming the presence of iron oxides, and the other two peaks at 531.8 and 533.7 eV correspond to O–C and O=C, respectively [24, 25].

The micromorphology and structure of CF, Fe<sub>2</sub>O<sub>3</sub>, CF@Fe<sub>2</sub>O<sub>3</sub>, and CF@Fe<sub>3</sub>O<sub>4</sub>@C using SEM and EDS are shown in Fig. 3. As can be seen from Fig. 3a, the shape of the electrospun fiber is smooth and regular with uniform diameter about 200–300 nm. The SEM image of CF is shown in Fig. 3b, the surface is smooth with fractures and bending, and the diameter has no obvious shrinkage or expansion. Figure 3c and d show the micromorphology of spindle-shaped particles of Fe<sub>2</sub>O<sub>3</sub> with regular shape and size consistency about 70 nm in diameter and 180 nm in length. Figure 3e and f exhibit the micromorphology of CF@Fe<sub>2</sub>O<sub>3</sub> that spindle-shaped Fe<sub>2</sub>O<sub>3</sub> grow uniformly on the CF surface upright, and the outline of CF is clearly visible. The shapes of CF@Fe<sub>3</sub>O<sub>4</sub>@C are shown in Fig. 3g and h. The outline of CF is still visible, and the iron oxide-coated carbon has lost the original spindle-like morphology and becomes the uniform spherical particles. Meanwhile, the thin film can be seen on the surface of the

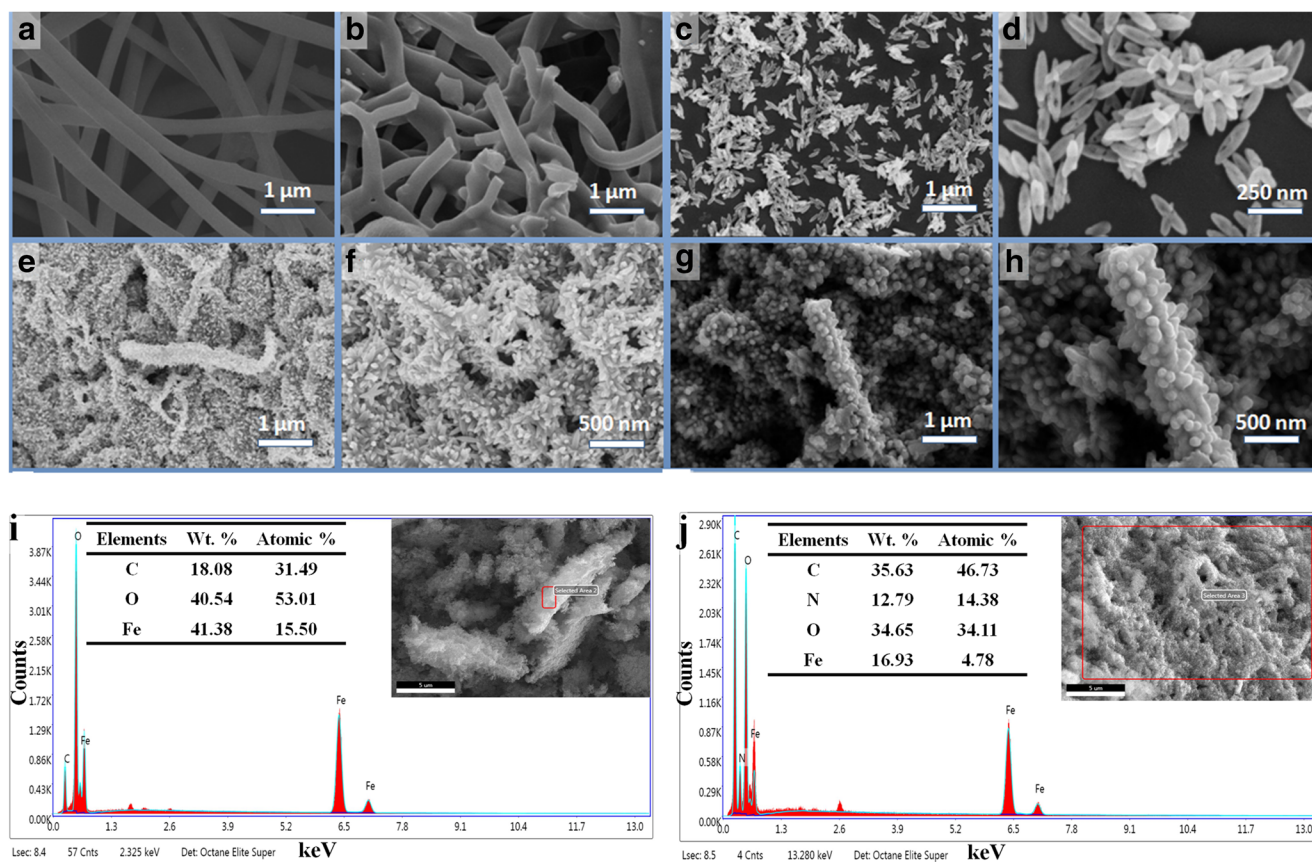


**Fig. 3** a SEM image of fibers by electrospinning. b SEM image of CF after heat treatment. c, d SEM images of Fe<sub>2</sub>O<sub>3</sub>. e, f SEM images of CF@Fe<sub>2</sub>O<sub>3</sub>. g, h SEM images of CF@Fe<sub>3</sub>O<sub>4</sub>@C; EDX spectrum of (i) CF@Fe<sub>2</sub>O<sub>3</sub> and (j) CF@Fe<sub>3</sub>O<sub>4</sub>@C

spheres, indicating that CF@Fe<sub>2</sub>O<sub>3</sub> is successfully coated with dopamine as a carbon source.

In order to determine the content of various elements in the composites, EDS analysis was performed on the samples CF@Fe<sub>2</sub>O<sub>3</sub> and CF@Fe<sub>3</sub>O<sub>4</sub>@C, and the results are shown in Fig. 3i and j. As shown in Fig. 3i, CF@Fe<sub>2</sub>O<sub>3</sub> is composed of Fe, O, and C elements, and the contents are 41.38 wt%, 40.54 wt%, and 18.08 wt% respectively. For Fig. 3j, CF@Fe<sub>3</sub>O<sub>4</sub>@C is composed of Fe, O, C, and N, and the contents are 16.93 wt%, 34.65 wt%, 35.63 wt%, and 12.79 wt% respectively. The comparison results show that the C element content increases significantly and N element content reaches 12.79 wt% obviously from dopamine hydrochloride of CF@Fe<sub>3</sub>O<sub>4</sub>@C.

The morphology and crystal structure of CF@Fe<sub>2</sub>O<sub>3</sub> and CF@Fe<sub>3</sub>O<sub>4</sub>@C were examined by TEM and HRTEM testing, and the results are shown in Fig. 4. In Fig. 4a, it can be seen that the spindle-shaped Fe<sub>2</sub>O<sub>3</sub> particles are clearly angular and uniformly arranged on the outer layer of CF. In Fig. 4b, the representative HRTEM image shows a lattice spacing of 0.369 nm corresponding to the lattice fringes of the α-Fe<sub>2</sub>O<sub>3</sub> (012) plane, indicating that the crystal α-Fe<sub>2</sub>O<sub>3</sub> is formed [26]. This result is consistent with the result of the XRD pattern. As shown in Fig. 4c, the edges and corners of the spindle-shaped

Fe<sub>2</sub>O<sub>3</sub> in CF@Fe<sub>3</sub>O<sub>4</sub>@C disappeared and transformed into spherical Fe<sub>3</sub>O<sub>4</sub> particles. The HRTEM image in Fig. 4d clearly shows that Fe<sub>3</sub>O<sub>4</sub> particles are uniformly coated with a layer of carbon material with a thickness about 8 nm. The selected area electron diffraction pattern in the embedded figure shows diffraction ring of Fe<sub>3</sub>O<sub>4</sub> on the (220), (311), (400), and (440), indicating that the crystal structure of Fe<sub>2</sub>O<sub>3</sub> carbon coating has transformed into Fe<sub>3</sub>O<sub>4</sub> after heat treatment. This result is also consistent with XRD pattern.

As shown in Fig. 5, the nitrogen adsorption-desorption isotherms and pore size distribution characteristics of CF, Fe<sub>2</sub>O<sub>3</sub>, CF@Fe<sub>2</sub>O<sub>3</sub>, and CF@Fe<sub>3</sub>O<sub>4</sub>@C were investigated. In Fig. 5a, the curve trend of CF is close to the H4 type hysteresis curve between 0 and 1.0 (P/P<sub>0</sub>), indicating that it contains narrow slotted pores. The specific surface area is 8.35 m<sup>2</sup> g<sup>-1</sup> and the average pore diameter is 3.42 nm. Figure 5b shows the results of Fe<sub>2</sub>O<sub>3</sub>; the curve trend is H3 type hysteresis curve.

There are more mesopores near 13 nm and 33 nm, its specific surface area is 38.25 m<sup>2</sup> g<sup>-1</sup>, and the average pore size is 7.29 nm. Figure 5c shows the results of CF@Fe<sub>2</sub>O<sub>3</sub>, and a hysteresis loop is close to the H3 type hysteresis curve. Its specific surface area is 33.40 m<sup>2</sup> g<sup>-1</sup> and the average pore size of 11.48 nm. The results of CF@Fe<sub>3</sub>O<sub>4</sub>@C are displayed in Fig. 5d, and the curve is close to the H5 type hysteresis curve

**Fig. 4** **a** TEM image and **b** HRTEM image of CF@Fe<sub>2</sub>O<sub>3</sub>, **c** TEM image and **d** HRTEM image and SAED patterns of CF@Fe<sub>3</sub>O<sub>4</sub>@C

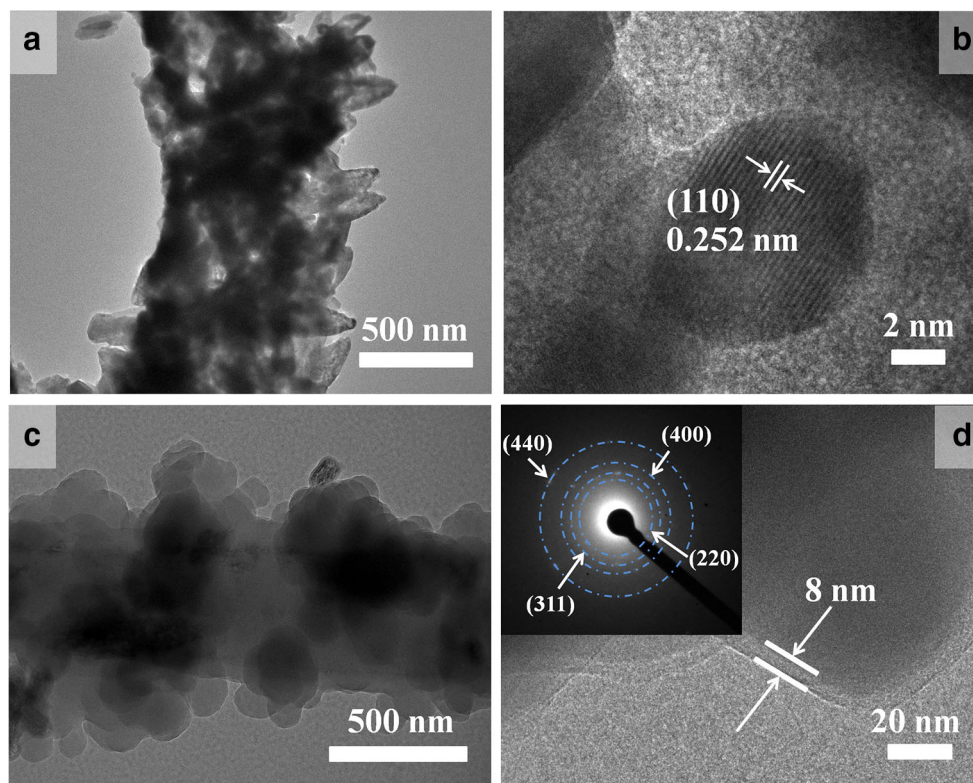
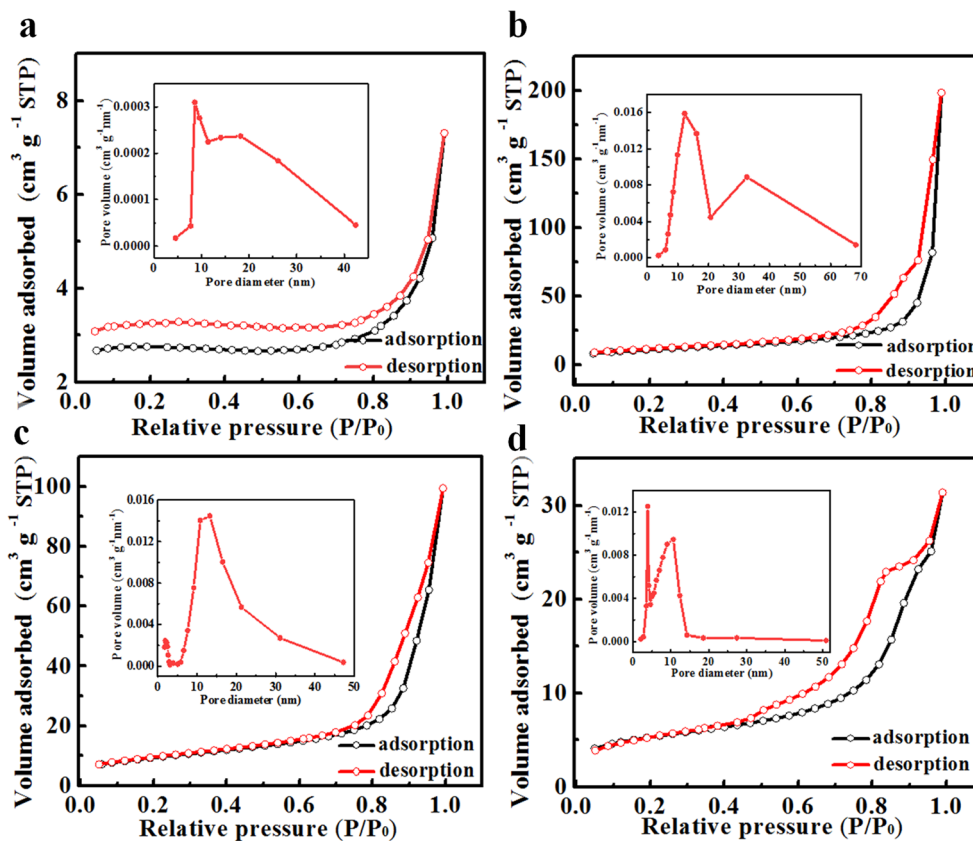


**Fig. 5** Nitrogen adsorption-desorption isotherms and pore size distribution of **a** CF, **b** Fe<sub>2</sub>O<sub>3</sub>, **c** CF@Fe<sub>2</sub>O<sub>3</sub>, and **d** CF@Fe<sub>3</sub>O<sub>4</sub>@C



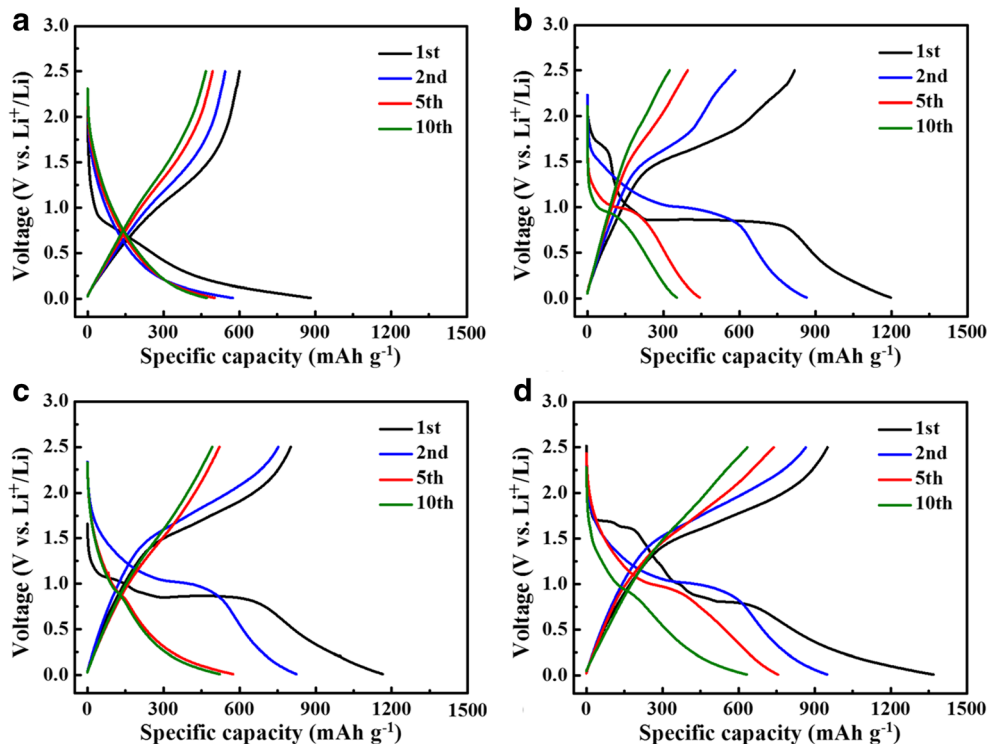
between 0.4 and 1.0. It is generally considered that this curve is common in mesoporous materials with partially blocked channels [27, 28]. The specific surface area becomes smaller to 17.91 m<sup>2</sup> g<sup>-1</sup> because those pores of CF@Fe<sub>2</sub>O<sub>3</sub> are partially filled with carbon coating.

The BJH results show that the average pore diameter is 8.28 nm. It is worth noting that the average pore size becomes smaller, especially the pore distributions in the range of 3–4 nm, comparing with CF@Fe<sub>2</sub>O<sub>3</sub> without carbon uncoated.

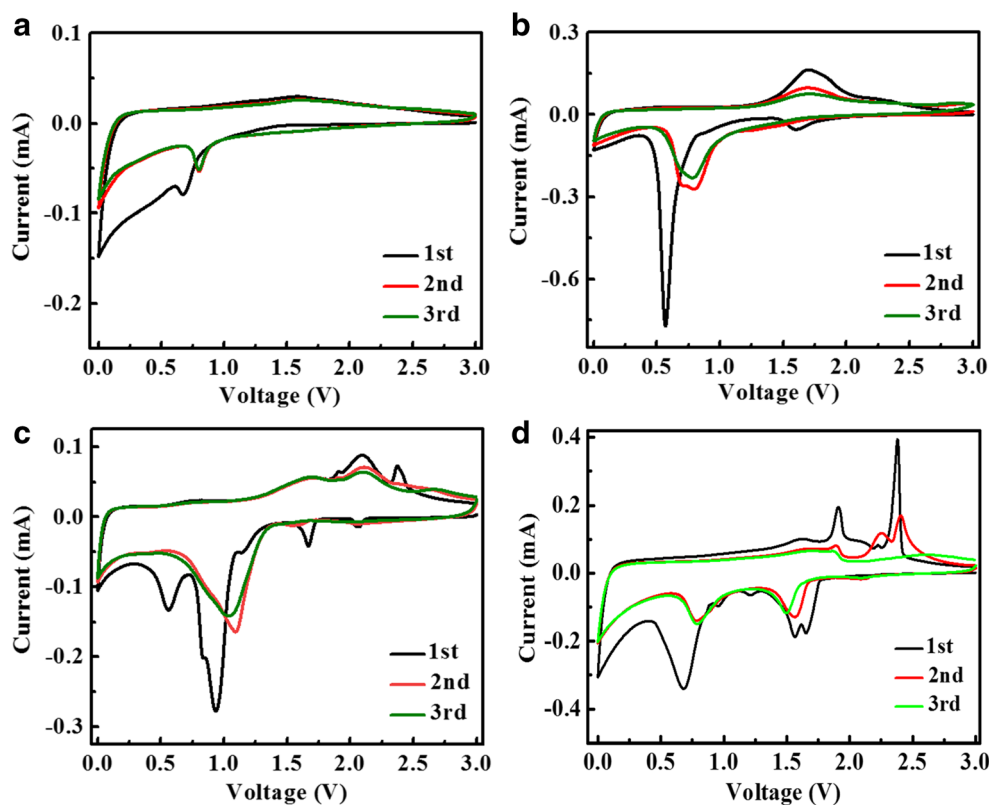
The galvanostatic charge-discharge curves of CF, Fe<sub>2</sub>O<sub>3</sub>, CF@Fe<sub>2</sub>O<sub>3</sub>, and CF@Fe<sub>3</sub>O<sub>4</sub>@C for the 1st, 2nd, 5th, and 10th cycles are shown in Fig 6. At current density of 100 mA g<sup>-1</sup> in the range of 0.01–2.5 V (vs. Li<sup>+</sup>/Li), the initial discharge/charge specific capacities are 882/601, 1198/818, 1164/801, and 1368/940 mAh g<sup>-1</sup>, respectively. After 10 cycles, Fe<sub>2</sub>O<sub>3</sub> shows the lowest discharge/charge specific capacity of 352/325 mAh g<sup>-1</sup>, which may be due to its structural instability and volume expansion leading to the loss of some electrode materials after charge/discharge cycles. The discharge/charge specific capacity of CF is relatively stable and keeps 471/468 mAh g<sup>-1</sup>. The specific capacity of CF@Fe<sub>2</sub>O<sub>3</sub> is 522/492 mAh g<sup>-1</sup>. The CF@Fe<sub>3</sub>O<sub>4</sub>@C has the highest discharge/charge specific capacity of 633/634 mAh g<sup>-1</sup>, and the coulomb efficiency is close to 100%. All these may be mainly due to the better conductivity from the carbon fiber and coated carbon layer, and Fe<sub>3</sub>O<sub>4</sub> has a relatively high theoretical specific capacity and the coated carbon layer can effectively alleviate volume expansion to restrain the capacity fading of the electrode material.

The first to third cycles of cyclic voltammetry (CV) curves of CF, Fe<sub>2</sub>O<sub>3</sub>, CF@Fe<sub>2</sub>O<sub>3</sub>, and CF@Fe<sub>3</sub>O<sub>4</sub>@C electrodes in 0.01–3.0 V (vs. Li<sup>+</sup>/Li) with the scan rate of 0.1 mV s<sup>-1</sup> are presented in Fig. 7. As shown in Fig. 7a, an obvious reduction peak in the first cathodic scan of CF appears near 0.7 V, corresponding to the process of reaction between C and Li to form LiC<sub>6</sub> and the decomposition of the electrolyte to form a solid electrolyte phase interface (SEI) film. The reduction peak gradually weakens in subsequent cycles and shifts to around 0.8 V. During the anodic scan, a weaker oxidation peak appears near 1.55 V, which is considered to be the oxidation process of C [29, 30]. For the CV curves of Fe<sub>2</sub>O<sub>3</sub> (Fig. 7b), the first sharp reduction peak at 0.56 V corresponds to the reduction of Fe<sup>3+</sup> and the formation of the SEI film and Li<sub>2</sub>O. The obvious reduction peak near 1.55 V can be attributed to the irreversible conversion of iron oxide. During the first anodic scan, a broad peak around 1.7 V corresponds to a reversible oxidation reaction and forming iron oxide and Li<sup>+</sup> [31, 32]. Figure 7c shows the CV curves of CF@Fe<sub>2</sub>O<sub>3</sub>, the reduction peaks at 0.55, 0.95, 1.65, and 2.1 V during the first cathodic scan. The strong reduction peak at 0.55 V corresponds to the reaction process of C and Li to form LiC<sub>6</sub>. The sharp reduction peak near 0.95 V corresponds to the reduction of Fe<sup>3+</sup> and the formation of the SEI film and Li<sub>2</sub>O. The weaker reduction peaks near 1.65 and 2.1 V can be attributed to the irreversible conversion of iron oxide. For the subsequent cycles, the reduction peaks mainly appear near 1.05 V. During the first anodic scan, there are two oxidation peaks at 1.68 V and 2.05 V, corresponding to the formation of iron oxide and

**Fig. 6** Galvanostatic discharge-charge curves of **a** CF, **b** Fe<sub>2</sub>O<sub>3</sub>, **c** CF@Fe<sub>2</sub>O<sub>3</sub>, and **d** CF@Fe<sub>3</sub>O<sub>4</sub>@C at 100 mA g<sup>-1</sup> in the range of 0.01–2.5 V (vs. Li<sup>+</sup>/Li)



**Fig. 7** CV curves of **a** CF, **b**  $\text{Fe}_2\text{O}_3$ , **c**  $\text{CF@Fe}_2\text{O}_3$ , and **d**  $\text{CF@Fe}_3\text{O}_4\text{@C}$



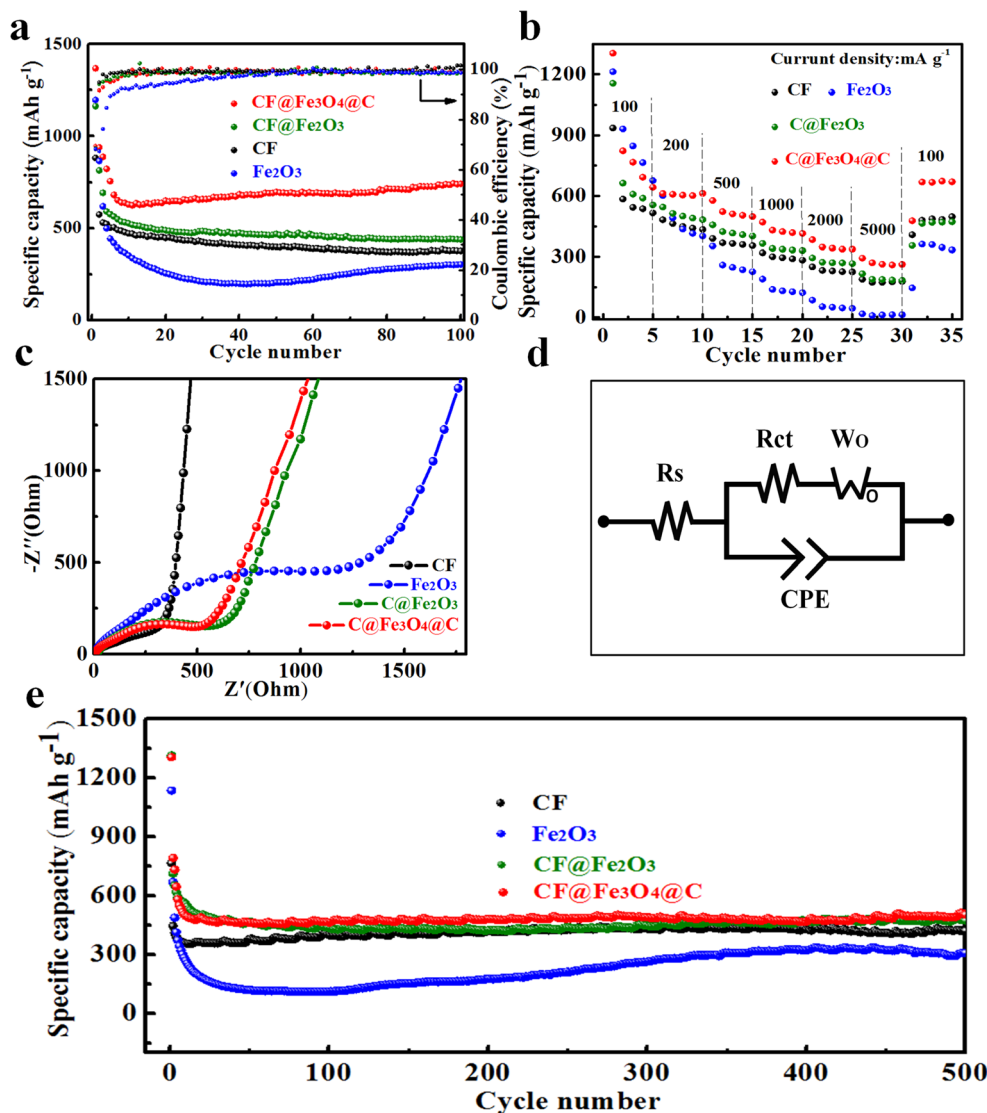
$\text{Li}^+$  [33–35]. The CV curves of  $\text{CF@Fe}_3\text{O}_4\text{@C}$  are shown in Fig. 7d, and strong reduction peaks appear at 0.7 and 1.6 V during the first cathodic scan, which correspond to the conversion of  $\text{Fe}^{3+}$  and  $\text{Fe}^{2+}$  to  $\text{Fe}^0$ , as well as the reaction of C and  $\text{Li}^+$  and the formation of a SEI film. In the subsequent two cathodic scan processes, the peaks gradually stabilize at 0.8 and 1.52 V, which can be attributed to the reversible reduction reaction of  $\text{Fe}^{3+}$  and  $\text{Fe}^{2+}$ . During the first anodic scan, strong peaks appear at 1.9 and 2.35 V, corresponding to the oxidation process of  $\text{Fe}^0$  to  $\text{Fe}^{2+}$  and  $\text{Fe}^{3+}$  with the reduction of  $\text{Li}^+$ . During the following anodic scans, the peak at 1.9 V becomes weak, corresponding to the process of  $\text{Fe}^0$  to form iron oxides. The strong peak disappeared near 2.35 V, indicating the presence of some irreversible reaction [36–38].

Figure 8a shows the specific capacity and coulomb efficiency curves of CF,  $\text{Fe}_2\text{O}_3$ ,  $\text{CF@Fe}_2\text{O}_3$ , and  $\text{CF@Fe}_3\text{O}_4\text{@C}$  electrodes at a current density of  $100 \text{ mA g}^{-1}$  in voltage of 0.01–2.5 V (vs.  $\text{Li}^+/\text{Li}$ ). It can be seen that the first discharge/charge specific capacities are 882/601, 1198/818, 1164/801, and 1368/940  $\text{mAh g}^{-1}$ , and the coulomb efficiencies are 68.1%, 68.3%, 68.8%, and 68.7%, respectively. After 100 cycles, the discharge/charge specific capacities are 376/376, 304/299, 438/436, and 741/740  $\text{mAh g}^{-1}$  and the coulomb efficiencies are 100%, 98.3%, 99.5%, and 99.8%, respectively. The specific capacity of  $\text{Fe}_2\text{O}_3$  declines continuously to 40 cycles and then begins to slowly rise. There are some possible reasons: (i) The increased charge

transfer kinetics in active materials enables new reactions after 40 cycles; (ii) The pulverization undergone by electrode materials during cycling leads to an increase in specific surface area; (iii) The morphology evolution during cycling gives rise to a reactivation of the electrochemical reaction [39]. The specific capacities of CF and  $\text{CF@Fe}_2\text{O}_3$  tend to stabilize after 10 cycles. Remarkably, the capacity of  $\text{CF@Fe}_3\text{O}_4\text{@C}$  gradually increases after 10 cycles that could be because  $\text{CF@Fe}_3\text{O}_4\text{@C}$  forms the channel structure for rapid lithium ion transfer after multiple charge/discharge. After the 100 cycles, the specific capacity of  $\text{Fe}_2\text{O}_3$  decays fastest, the reason is that the volume expansion during charging/discharging causes the active material to detach from the current collector. It is worth noting that  $\text{CF@Fe}_3\text{O}_4\text{@C}$  not only has carbon fibers that increase the conductivity of iron oxides but also has the coated carbon layer that can effectively improve the specific capacity fading caused by volume expansion. Furthermore, the mesoporous distribution in the range of 3–4 nm provided more active reaction sites and also helped to increase the specific capacity. The formation and activation of a stable SEI layer with repeatedly absorbing and releasing lithium ions caused the gradual penetration of electrolyte over the porous active material during cycling and the progressive generation of electrochemical active polymeric films, leading to gradually increase of the specific capacity [40]. This phenomenon is particularly obvious at low current densities [41–45].



**Fig. 8** **a** Specific capacity and coulombic efficiency after 100 cycles at 100 mA g<sup>-1</sup> in the range of 0.01~2.5 V (vs. Li<sup>+</sup>/Li). **b** Rate performance, **c** electrochemical impedance spectroscopy (EIS), and **d** equivalent circuit model for the fitting of the Nyquist plots and cycle stability at 500 mA g<sup>-1</sup> in the range of 0.01~2.5 V (vs. Li<sup>+</sup>/Li)



The rate performance results of CF, Fe<sub>2</sub>O<sub>3</sub>, CF@Fe<sub>2</sub>O<sub>3</sub>, and CF@Fe<sub>3</sub>O<sub>4</sub>@C electrodes are shown in Fig. 8b. The current densities were 100, 200, 500, 1000, 2000, and 5000 mA g<sup>-1</sup>, and then returned to 100 mA g<sup>-1</sup>. As can be clearly seen from the figure, the discharge specific capacities of four electrodes displayed a gradual decrease with the current density increase. The polarization effect of the electrode materials becomes larger and the deposition of Li<sup>+</sup> becomes more pronounced due to the current increasing. The average discharge specific capacities were 178, 14, 192, and 270 mAh g<sup>-1</sup> respectively at the current density of 5 A g<sup>-1</sup>, and which returned to 471, 309, 446, and 631 mAh g<sup>-1</sup> respectively when the current density was restored to 100 mA g<sup>-1</sup>, indicating that CF@Fe<sub>3</sub>O<sub>4</sub>@C electrode has better rate performance and reversible performance. The reason may be that carbon fiber improves the electrical conductivity, providing

CF@Fe<sub>3</sub>O<sub>4</sub>@C electrode with fast electrochemical kinetics, low internal resistance, and fast charge transfer capacity [46, 47]. In addition, the Fe<sub>3</sub>O<sub>4</sub> provides high specific capacity, and the carbon coated on the surface relieves the volume expansion of Fe<sub>3</sub>O<sub>4</sub> during the charge/discharge cycles [48].

Figure 8c presents the initial electrochemical impedance spectroscopy (EIS) of CF, Fe<sub>2</sub>O<sub>3</sub>, CF@Fe<sub>2</sub>O<sub>3</sub>, and CF@Fe<sub>3</sub>O<sub>4</sub>@C, respectively. All the Nyquist plots are consisted of high-frequency semicircles and low-frequency sloping lines. In general, the high-frequency semicircle indicates the solid electrolyte interface resistance or SEI film and the straight line is associated with ion diffusion resistance [15, 49, 50]. It can be seen from the figure that the semicircle of CF electrode is the smallest, and the semicircle of CF@Fe<sub>3</sub>O<sub>4</sub>@C is smaller than Fe<sub>2</sub>O<sub>3</sub> and CF@Fe<sub>2</sub>O<sub>3</sub>. This indicates that the charge transfer resistance and the electrolyte or surface resistance of CF is the smallest, that

of CF@Fe<sub>3</sub>O<sub>4</sub>@C and CF@Fe<sub>2</sub>O<sub>3</sub> is similar and smaller, and that of Fe<sub>2</sub>O<sub>3</sub> is the largest. As shown in Fig. 8d, the equivalent circuit model is composed of the constant phase element (CPE<sub>ct</sub>) associated with electrode double-layer capacitance, the Warburg element (*W*<sub>o</sub>) associated with Li ion diffusion in the electrode, the electrolyte resistance (*R*<sub>s</sub>), and the charge transfer resistance (*R*<sub>ct</sub>) [19, 25]. The *R*<sub>ct</sub> values of CF, Fe<sub>2</sub>O<sub>3</sub>, CF@Fe<sub>2</sub>O<sub>3</sub>, and CF@Fe<sub>3</sub>O<sub>4</sub>@C are 274 Ω, 753 Ω, 482 Ω, and 396 Ω, respectively. It is obvious that the *R*<sub>ct</sub> of CF@Fe<sub>3</sub>O<sub>4</sub>@C is smaller than that of Fe<sub>2</sub>O<sub>3</sub> and CF@Fe<sub>2</sub>O<sub>3</sub>, showing the faster charge-transfer reaction for Li<sup>+</sup> insertion and extraction than Fe<sub>2</sub>O<sub>3</sub> and CF@Fe<sub>2</sub>O<sub>3</sub> electrode. It can be seen that the introduction of carbon fiber and shell could further increase the electronic conductivity and result in the enhanced reaction kinetics of electrode materials.

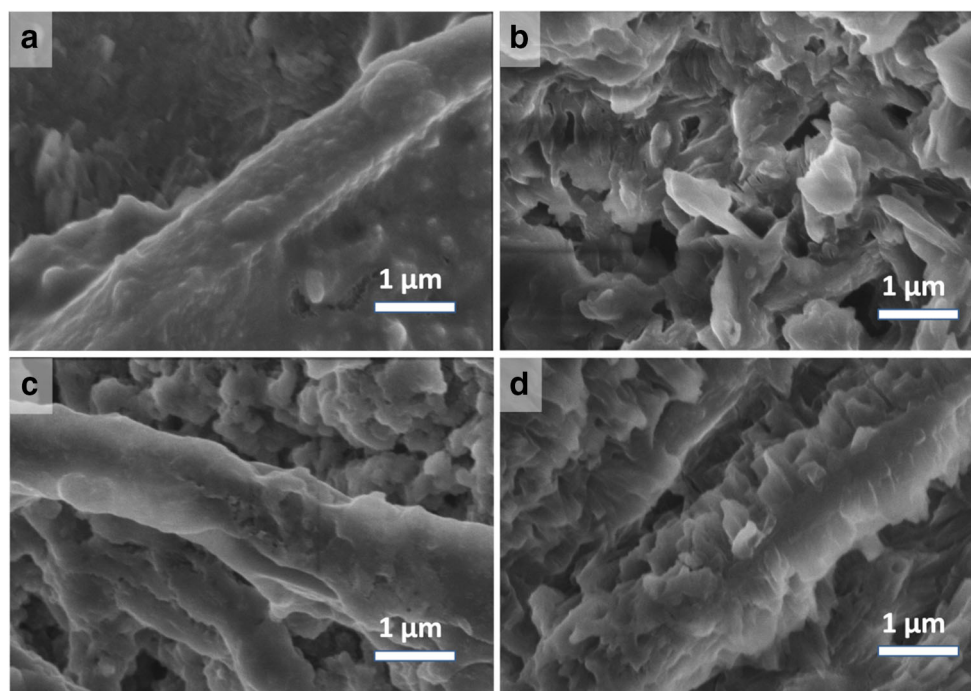
Furthermore, to understand the charge/discharge performance of the electrode materials at a large current and long cycle, the discharge specific capacities of 500 cycles were carried out at a current density of 500 mA g<sup>-1</sup> in 0.01~2.5 V (vs. Li<sup>+</sup>/Li). As shown in Fig. 8e, all the specific capacities decrease with the increasing cycling, and Fe<sub>2</sub>O<sub>3</sub> is the smallest. After 90 cycles, it decayed to a minimum (110 mAh g<sup>-1</sup>), then increased slightly and stabilized about 308 mAh g<sup>-1</sup> until 500 cycles. The discharge specific capacities of CF, CF@Fe<sub>2</sub>O<sub>3</sub>, and CF@Fe<sub>3</sub>O<sub>4</sub>@C have generally stabilized after 50 cycles, which were 421, 474, and 503 mAh g<sup>-1</sup> after 500 cycles, respectively.

It can be seen that the CF@Fe<sub>3</sub>O<sub>4</sub>@C electrode has higher cycle stability performance at a large current density.

In order to investigate the stability of the electrode structure, the surface morphology of CF, Fe<sub>2</sub>O<sub>3</sub>, CF@Fe<sub>2</sub>O<sub>3</sub>, and CF@Fe<sub>3</sub>O<sub>4</sub>@C electrodes was observed by SEM. The SEM images of samples after 500 cycles at a current density of 500 mA g<sup>-1</sup> are shown in Fig. 9. According to the comparison between the results in Fig. 9 and the SEM images before cycling in Fig. 3, it can be seen clearly that the spindle-shaped Fe<sub>2</sub>O<sub>3</sub> of CF@Fe<sub>2</sub>O<sub>3</sub> outer layer and spherical particle Fe<sub>3</sub>O<sub>4</sub> of CF@Fe<sub>3</sub>O<sub>4</sub>@C cannot be observed. Not only the particles of Fe<sub>2</sub>O<sub>3</sub> but also the fiber-like electrode materials of CF, CF@Fe<sub>2</sub>O<sub>3</sub>, and CF@Fe<sub>3</sub>O<sub>4</sub>@C have almost doubled in size compared with the original. The surface of particles and fiber active materials was covered with a layer of SEI film, which also confirmed the results of the SEI film generated in the CV test results. More importantly, it can be clearly seen from Fig. 9a, c, and d that the active materials still remain fibers shape after 500 cycles, indicating that the electrode materials can still maintain the structural integrity, rarely falling off and collapsing.

They were in a good working condition, which can confirm the specific capacities of CF, CF@Fe<sub>2</sub>O<sub>3</sub>, and CF@Fe<sub>3</sub>O<sub>4</sub>@C electrode materials were stable after long-term charging and discharging cycles. In Fig. 9b, the original spindle-shaped Fe<sub>2</sub>O<sub>3</sub> particles were severely broken, which can also explain the specific capacity decayed faster during the charging/discharging cycles. In short, from this result, the CF@Fe<sub>3</sub>O<sub>4</sub>@C electrode material has good reversible cycling performance in terms of structural stability.

**Fig. 9** SEM images of **a** CF, **b** Fe<sub>2</sub>O<sub>3</sub>, **c** CF@Fe<sub>2</sub>O<sub>3</sub>, and **d** CF@Fe<sub>3</sub>O<sub>4</sub>@C after 500 cycles at 500 mA g<sup>-1</sup>



## Conclusion

In summary, we designed and synthesized mace-like CF@Fe<sub>3</sub>O<sub>4</sub>@C composites by an in situ growth and carbon coating approach with heat treatment. Comparison with CF, Fe<sub>2</sub>O<sub>3</sub>, and CF@Fe<sub>2</sub>O<sub>3</sub>, it is discovered that CF@Fe<sub>3</sub>O<sub>4</sub>@C composites display higher electrochemical performance (such as reversible capacity, rate performance, and long cycle performance). At 100 mA g<sup>-1</sup> in the range of 0.01–2.5 V, the discharge/charge specific capacities at the first and 100th cycles are 1368/940 mAh g<sup>-1</sup> and 741/740 mAh g<sup>-1</sup>. The specific discharge capacity can still retain 503 mAh g<sup>-1</sup> after 500 cycles at 500 mA g<sup>-1</sup>. It can be attributed to that carbon fibers and carbon coating improve the electrical conductivity of iron oxides and carbon-coated layer avoids the specific capacity fading caused by volume expansion of iron oxides during charging/discharging. It provides an effective synthesis method and structural design strategy of anode material for high-energy lithium-ion battery.

**Funding** This work was supported by the National Science Foundation of China (51603147) and Tianjin application foundation and advanced technology research plan project (15ZCZDZX00270 and 14RCHZGX00859).

## References

- Xu ZR, Gao LB, Liu YJ, Li L (2016) Review-recent developments in the doped LiFePO<sub>4</sub> cathode materials for power lithium ion batteries. *J Electrochem Soc* 163(13):2600–2610
- Li M, Lu J, Chen ZW, Amine K (2018) 30 years of lithium-ion batteries. *Adv Mater* 30(33):1800561
- Zhao Y, Li XF, Yan B, Xiong DB, Li DJ, Lawes S (2015) Recent developments and understanding of novel mixed transition-metal oxides as anodes in lithium ion batteries. *Adv Energy Mater* 5(23):1501106
- Tarascon JM, Armand M (2001) Issues and challenges facing rechargeable lithium batteries. *Nature* 414:359–367
- Gao G, Zhang Q, Cheng XB, Qiu PY, Sun RJ, Yin T, Cui DX (2015) CNTs in situ attached to  $\alpha$ -Fe<sub>2</sub>O<sub>3</sub> submicron spheres for enhancing lithium storage capacity. *ACS Appl Mater Interfaces* 7(1):340–350
- Dwivedi PK, Muniraj VKA, Devarapalli RR, Shelke MV (2018) Ni(OH)<sub>2</sub>-Fe<sub>2</sub>O<sub>3</sub>/CNOs ternary nanocomposite designed as an anode with complementary properties for high-performance Li-ion battery. *ChemistrySelect* 3(8):2286–2292
- Zhou S, Zhou Y, Jiang W, Guo HJ, Wang ZX, Li XH (2018) Synthesis of Fe<sub>3</sub>O<sub>4</sub> cluster microspheres/graphene aerogels composite as anode for high-performance lithium ion battery. *Appl Surf Sci* 439:927–933
- Hang BT, Okadab S, Yamaki JI (2008) Effect of binder content on the cycle performance of nano-sized Fe<sub>2</sub>O<sub>3</sub>-loaded carbon for use as a lithium battery negative electrode. *J Power Sources* 178:402–408
- Lei Y, Li J, Wang YY, Gu L, Chang YF, Yuan HY, Xiao D (2014) Rapid microwave-assisted green synthesis of 3D hierarchical flower-shaped NiCo<sub>2</sub>O<sub>4</sub> microsphere for high-performance supercapacitor. *ACS Appl Mater Interfaces* 6(3):1773–1780
- Li H, Ma HR, Yang M, Wang B, Shao H, Wang L, Yu RB, Wang D (2017) Highly controlled synthesis of multi-shelled NiO hollow microspheres for enhanced lithium storage properties. *Mater Res Bull* 87:224–229
- Wang Y, Roller J, Maric R (2018) Novel flame synthesis of nanostructured  $\alpha$ -Fe<sub>2</sub>O<sub>3</sub> electrode as high performance anode for lithium ion batteries. *J Power Sources* 378:511–515
- Zhao YJ, Yan D, Ding CH, Su DZ, Ge YY, Zhao YZ, Zhou HP, Li JB, Jin HB (2016) Fe<sub>2</sub>O<sub>3</sub> nanocubes exposed (012) active facets combination with graphene rendering enhanced lithium storage capability. *J Power Sources* 327:658–665
- Zhang WM, Wu XL, Hu JS, Guo YG, Wan LJ (2008) Carbon coated Fe<sub>3</sub>O<sub>4</sub> nanospindles as a superior anode material for lithium-ion batteries. *Adv Funct Mater* 18(24):3941–3946
- Liu XN, He G, Li JS, Yin GF (2017) The synthesis and mechanism of (001)-orientated hematite nano rings: a combined theoretical and experimental investigation. *Nano* 12(9):1750111
- Park GD, Hong JH, Jung DS, Lee JH, Kang YC (2019) Unique structured microspheres with multishells comprising graphitic carbon-coated Fe<sub>3</sub>O<sub>4</sub> hollow nanopowders as anode materials for high performance Li-ion batteries. *J Mater Chem A* 7(26):15766–15773
- Deng W, Ci SQ, Li H, Wen ZH (2017) One-step ultrasonic spray route for rapid preparation of hollow Fe<sub>3</sub>O<sub>4</sub>/C microspheres anode for lithium-ion batteries. *Chem Eng J* 330:995–1001
- Cherian CT, Sundaramurthy J, Kalaivani M, Ragupathy P, Kumar PS, Thavasi V, Reddy MV, Sow CH, Mhaisalkar SG, Ramakrishna S, Chowdari BVR (2012) Electrospun  $\alpha$ -Fe<sub>2</sub>O<sub>3</sub> nanorods as a stable, high capacity anode material for Li-ion batteries. *J Mater Chem* 22(24):12198–12204
- Nasibulin AG, Rackauskas S, Jiang H, Tian Y, Mudimela PR, Shandakov SD, Nasibulina L, Sainio J, Kauppinen EI (2009) Simple and rapid synthesis of  $\alpha$ -Fe<sub>2</sub>O<sub>3</sub> nanowires under ambient conditions. *Nano Res* 2(5):373–379
- Jiang Y, Jiang ZJ, Yang LF, Cheng S, Liu ML (2015) A high-performance anode for lithium ion batteries: Fe<sub>3</sub>O<sub>4</sub> microspheres encapsulated in hollow graphene shells. *J Mater Chem A* 3(22):11847–11856
- Wang Y, Guo XM, Wang ZK, Lü MF, Wu B, Wang Y, Yan C, Yuan AH, Yang HX (2017) Controlled pyrolysis of MIL-88A to Fe<sub>2</sub>O<sub>3</sub>@C nanocomposites with varied morphologies and phases for advanced lithium storage. *J Mater Chem A* 5(48):25562–25573
- Luo D, Deng YP, Wang XL, Li GR, Wu J, Lei W, Liang RL, Liu YS, Ding YL, Yu AP, Chen ZW (2017) Tuning shell numbers of transition metal oxide hollow microspheres toward durable and superior lithium storage. *ACS Nano* 11(11):11521–11530
- Zheng FC, He MN, Yang Y, Chen QW (2015) Nano electrochemical reactors of Fe<sub>2</sub>O<sub>3</sub> nanoparticles embedded in shells of nitrogen-doped hollow carbon spheres as high-performance anodes for lithium-ion batteries. *Nanoscale* 7(8):3410–3417
- Yang Z, Su DY, Yang JP, Wang J (2017) Fe<sub>3</sub>O<sub>4</sub>/C composite with hollow spheres in porous 3D-nanostructure as anode material for the lithium-ion batteries. *J Power Sources* 363:161–167
- Liu XD, Fan HT, Li B, Hu M, Hu YT, Liu M, Liu GY, Ma JM (2019)  $\alpha$ -Fe<sub>2</sub>O<sub>3</sub> hollow microspheres assembled by ultrathin nanoflakes exposed with (241) high-index facet: solvothermal synthesis, lithium storage performance, and superparamagnetic property. *Int J Hydrog Energy* 44(2):1070–1077
- Ai Q, Yuan ZW, Huang RZ, Yang CX, Jiang GD, Xiong J, Huang Z, Yuan SD (2019) One-pot co-precipitation synthesis of Fe<sub>3</sub>O<sub>4</sub> nanoparticles embedded in 3D carbonaceous matrix as anode for lithium ion batteries. *J Mater Sci* 54(5):4212–4224
- Wang B, Chen JS, Lou XW (2012) The comparative lithium storage properties of urchin-like hematite spheres: hollow vs. solid. *J Mater Chem* 22:9466–9468

27. Zhao XX, Yu RB, Tang HJ, Mao D, Qi J, Wang B, Zhang Y, Zhao HJ, Hu WP, Wang D (2017) Formation of septuple-shelled  $(\text{Co}_{2.3}\text{Mn}_{1.3})(\text{Co}_{5.6}\text{Mn}_{1.6})_2\text{O}_4$  hollow spheres as electrode material for alkaline rechargeable battery. *Adv Mater* 29(34):1700550
28. Xu SM, Hessel CM, Ren H, Yu RB, Jin Q, Yang M, Zhao HJ, Wang D (2014)  $\alpha\text{-Fe}_2\text{O}_3$  multi-shelled hollow microspheres for lithium ion battery anodes with superior capacity and charge retention. *Energy Environ Sci* 7(2):632–637
29. Kim C, Yang KS, Kojima M, Yoshida K, Kim YJ, Kim YA, Endo M (2006) Fabrication of electrospinning-derived carbon nanofiber webs for the anode material of lithium-ion secondary batteries. *Adv Funct Mater* 16(18):2393–2397
30. Lee JK, An KW, Ju JB, Cho BW, Cho WI, Park D, Yun KS (2001) Electrochemical properties of PAN-based carbon fibers as anodes for rechargeable lithium ion batteries. *Carbon* 39(9):1299–1305
31. Chaudhari NK, Kim MS, Bae TS, Yu JS (2013) Hematite ( $\alpha\text{-Fe}_2\text{O}_3$ ) nanoparticles on vulcan carbon as an ultrahighcapacity anode material in lithium ion battery. *Electrochim Acta* 114:60–67
32. Li Y, Zhu CL, Lu T, Guo ZP, Zhang D, Ma J, Zhu SM (2013) Simple fabrication of a  $\text{Fe}_2\text{O}_3$ /carbon composite for use in a high-performance lithium ion battery. *Carbon* 52:565–573
33. Chen MH, Liu JL, Chao DL, Wang J, Yin JH, Lin JY, Fan HJ, Shen ZX (2014) Porous  $\alpha\text{-Fe}_2\text{O}_3$  nanorods supported on carbon nanotubes-graphene foam as superior anode for lithium ion batteries. *Nano Energy* 9:364–372
34. Cho JS, Hong YJ, Kang YC (2015) Design and synthesis of bubble-nanorod-structured  $\text{Fe}_2\text{O}_3$ /carbon nanofibers as advanced anode material for Li-ion batteries. *ACS Nano* 9(4):4026–4035
35. Wu CY, Li XP, Li WS, Li B, Wang YQ, Wang YT, Xu MQ, Xing LD (2014)  $\text{Fe}_2\text{O}_3$  nanorods/carbon nanofibers composite: preparation and performance as anode of high rate lithium ion battery. *J Power Sources* 251:85–91
36. Zhao L, Gao MM, Yue WB, Jiang Y, Wang Y, Ren Y, Hu FQ (2015) Sandwich-structured graphene- $\text{Fe}_3\text{O}_4$ @carbon nanocomposites for high-performance lithium-ion batteries. *ACS Appl Mater Interfaces* 7(18):9709–9715
37. Wang Y, Chen L, Liu HT, Xiong ZM, Zhao L, Liu SH, Huang CM, Zhao YM (2019) Cornlike ordered N-doped carbon coated hollow  $\text{Fe}_3\text{O}_4$  by magnetic self-assembly for the application of Li-ion battery. *Chem Eng J* 356:746–755
38. Han WJ, Qin XY, Wu JX, Li Q, Liu M, Xia Y, Du HD, Li BH, Kang FY (2018) Electrospayed porous  $\text{Fe}_3\text{O}_4$ /carbon microspheres as anode materials for high-performance lithium-ion batteries. *Nano Res* 11(2):892–904
39. Kim H, Choi W, Yoon J, Um JH, Lee W, Kim J, Cabana J, Yoon WS (2020) Exploring anomalous charge storage in anode materials for next-generation Li rechargeable batteries. *Chem Rev* 120(14):6934–6976
40. Huang M, Mi K, Zhang JH, Liu HL, Yu TT, Yuan AH, Kong QH, Xiong SL (2017) MOFs-derived Bi-metal embedded N-doped carbon polyhedral nanocages with enhanced lithium storage. *J Mater Chem A* 5(1):266–274
41. Li XW, Qiao L, Li D, Wang XH, Xie WH, He DY (2013) Three-dimensional network structured  $\alpha\text{-Fe}_2\text{O}_3$  made from a stainless steel plate as a high-performance electrode for lithium ion batteries. *J Mater Chem A* 1(21):6400–6406
42. Yu WJ, Zhang LL, Hou PX, Li F, Liu C, Cheng HM (2016) High reversible lithium storage capacity and structural changes of  $\text{Fe}_2\text{O}_3$  nanoparticles confined inside carbon nanotubes. *Adv Energy Mater* 6(3):1501755
43. Han F, Ma LJ, Sun Q, Lei C, Lu AH (2014) Rationally designed carbon-coated  $\text{Fe}_3\text{O}_4$  coaxial nanotubes with hierarchical porosity as high-rate anodes for lithium ion batteries. *Nano Res* 7(11):1706–1717
44. Luo JS, Liu JL, Zeng ZY, Ng CF, Ma LJ, Zhang H, Lin JY, Shen ZX, Fan HJ (2013) Three-dimensional graphene foam supported  $\text{Fe}_3\text{O}_4$  lithium battery anodes with long cycle life and high rate capability. *Nano Lett* 13(12):6136–6143
45. Wei W, Yang SB, Zhou HX, Lieberwirth I, Feng XL, Müllen K (2013) 3D graphene foams cross-linked with pre-encapsulated  $\text{Fe}_3\text{O}_4$  nanospheres for enhanced lithium storage. *Adv Mater* 25(21):2909–2914
46. Zhong W, Chen QW, Liu Z, Yang F, Liu WL, Sun KL, Kong FG, Ren MM (2020) Spindle-shaped core-shell  $\text{Fe}_3\text{O}_4$ @N-doped carbon composites scattered in graphene as excellent anode materials for lithium/sodium ion battery. *J Alloys Compd* 832:154879
47. Chen QW, Zhong W, Zhang JN, Gao CL, Liu WL, Li GD, Ren MM (2019)  $\text{Fe}_3\text{O}_4$  nanorods in N-doped carbon matrix with pseudo-capacitive behaviors as an excellent anode for subzero lithium-ion batteries. *J Alloys Compd* 772:557–564
48. Chen K, Kong XZ, Chen J, Cao XX, Liang SQ, Pan AQ (2020) Sulfur-doped carbon wrapped heterogeneous  $\text{Fe}_3\text{O}_4/\text{Fe}_7\text{S}_8/\text{C}$  nanoplates as stable anode for lithium ion batteries. *Batteries & Supercaps* 3(4):344–353
49. Bengono DAM, Zhang B, Yao YY, Tang LB, Yu WJ, Zheng JC, Chu DW, Li JY, Tong H (2020)  $\text{Fe}_3\text{O}_4$  wrapped by reduced graphene oxide as a high-performance anode material for lithium-ion batteries. *Ionics* 26:1695–1701
50. Liang CL, Li JL, Tian Q, Lin QQ, Bao RY, Liu Y, Peng XF, Yang MB, Yang W (2019) Nitrogen-doped carbon-coated  $\text{Fe}_3\text{O}_4$ /rGO nanocomposite anode material for enhanced initial coulombic efficiency of lithium-ion batteries. *Ionics* 25:1513–1521

**Publisher's note** Springer Nature remains neutral with regard to jurisdictional claims in published maps and institutional affiliations.